Available online at www.sciencedirect.com

ScienceDirect

IFAC PapersOnLine 58-20 (2024) 79–86

Unifying the Generalized Jacobian Matrix and prioritized task hierarchies, with application to free-floating VMSs ⋆

Marianna Wrzos-Kaminska * **Bjørn Kåre Sæbø** * **Kristin Y. Pettersen** * **Jan Tommy Gravdahl** *

* *Department of Engineering Cybernetics, Norwegian University of Science and Technology (NTNU), Trondheim, Norway (e-mail: {marianna.wrzos-kaminska, bjorn.k.sabo, kristin.y.pettersen, jan.tommy.gravdahl}@ntnu.no).*

Abstract: Free-floating vehicle manipulator systems (VMSs), such as those in space or underwater, experience a coupling effect between the motion of the manipulator arm and the vehicle base, since the motion of the joints induces a motion of the base relative to the system's center of gravity (CG). In this work a control framework is proposed that takes this coupling effect into account, selecting the motion of the CG as the highest priority task in a dynamically consistent task hierarchy in order to reduce the need for counteracting disturbances while controlling the position of the manipulator workspace. The proposed approach generalizes previous works using the Generalized Jacobian matrix to allow the completion of several prioritized tracking tasks. Control allocation is performed in a manner ensuring that the thrusters are used only for controlling the overall position of the VMS, while the joints are used for tasks requiring higher accuracy. The set in which all tracking error dynamics are zero is shown to be uniformly asymptotically stable, and the performance of the proposed control method is validated in a simulation study.

Keywords: Maritime robotics, nonlinear control, autonomous underwater vehicles, vehicle-manipulator systems, multitask control, redundant robots

1. INTRODUCTION

Uncrewed vehicles are increasingly used for exploring the oceans and gain access to their resources, for example to survey, explore caves or shipwrecks, or for inspection, maintenance and repair of subsea infrastructure. Underwater vehicle-manipulator systems (UVMSs) are vehicles equipped with some manipulator, frequently a jointed arm, enabling them to interact with their surroundings. Smaller, lighter vehicles are easier and cheaper to deploy, and small or slender vehicles have better access to e.g. caves, wrecks or underwater infrastructure. The articulated intervention autonomous underwater vehicle (AIAUV) is a vehicle with a slender, articulated body with thrusters mounted on its links, and can be used like a free-floating manipulator arm.

The literature on control of UVMSs has focused largely on vehicle-manipulator systems (VMSs) with a large, heavy vehicle base, and control schemes in which coordination of the vehicle and manipulator is performed on a kinematic level only, while the dynamics of each are controlled separately (Antonelli, 2018). Such an approach is satisfactory for these VMSs with a large, heavy base which does not experience much disturbance from the manipulator. However, free-floating VMSs with a comparably lighter vehicle base are more vulnerable to such disturbances, sometimes referred to as reaction forces (Umetani and Yoshida, 1989), where the motion of the manipulator arm induces a motion of the vehicle base. This occurs because it is the center of gravity (CG) of the vehicle that stays in place, while the joint motion changes the position of the vehicle base relative to the CG. For VMSs with a light base, the manipulator arm constitutes a larger part of their total mass, and therefore they are more vulnerable to this reaction effect. The effect is illustrated in Fig. 1, which shows the result of the same joint motion on a fixed-base manipulator, a free-floating VMS with a heavy base, and a free-floating VMS with a relatively light or no distinct base. Such effects were also observed by Borlaug et al. (2021) in experiments with an AIAUV, in which joint motion at the front of the vehicle disturbed the pose of its backmost link, despite

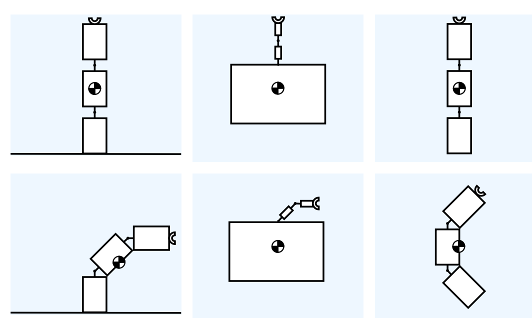

Fig. 1. The same joint motion performed by (left to right): a fixed-base manipulator, a free-floating VMS with a heavy base, and a free-floating VMS with a light base.

⋆ This project has received funding from the European Research Council (ERC) under the European Union's Horizon 2020 research and innovation programme, through the ERC Advanced Grant 101017697-CRÈME. The work is also supported by the Research Council of Norway through the Centres of Excellence funding scheme, project No. 223254 – NTNU AMOS.

10.1016/j.ifacol.2024.10.036

controlling its pose using a scheme designed to be robust against disturbances and uncertainties. This demonstrates the need to take these effects into account when designing control schemes for objectives requiring high precision.

To accurately control the end-effector of a free-floating VMS in space despite the induced motion of the vehicle base, the generalized Jacobian matrix (GJM) was introduced by Umetani and Yoshida (1989). It is a means of including some knowledge of the system dynamics, specifically its inertia, into kinematic control schemes. The GJM is derived based on conservation of momentum, thanks to which the induced motion of the base can be calculated and compensated for. Nakanishi and Yoshida (2006) use the GJM for impedance control at the end-effector. They provide both a velocity-level and torque-level control law, the latter based on cancellation of dynamics in order to achieve the desired acceleration at the end-effector. Kinematic control using the GJM has also been performed on an AIAUV by Amundsen et al. (2018) with promising simulation results.

The dynamics of floating-base robots were investigated by Garofalo et al. (2015), who derived them in terms of the total momentum and joint velocities as coordinates. This choice of coordinates is shown to result in inertial decoupling of their dynamics, and the GJM is derived as a special case when total momentum is zero. Similar coordinate transformations were used by Giordano et al. (2016, 2018) to develop a series of dynamic control laws for regulation of the end-effector pose of VMSs in space, taking into account situations in which total momentum of the system is not conserved. Thrusters are used to move the position of the CG of the system, but are not engaged to perform end-effector motion in order to conserve fuel. Manipulators which are redundant with respect to the task of controlling the end-effector pose were considered by Giordano et al. (2016). The null-space velocities, i.e. manipulator motion which does not contribute to neither end-effector velocity or total momentum, are dynamically decoupled from the end-effector motion so that they do not disturb it, but are not employed to perform any additional tasks. A similar approach has also been applied to an aerial VMS consisting of a helicopter with a comparably heavy arm attached to it by Garofalo et al. (2018), to ensure that control objectives to be performed by the manipulator arm do not disturb the position of the CG of the overall system and the attitude of the base vehicle.

The use of null-space projections is a well-established approach to solving the more general problem of utilizing all available degrees of freedom (DOFs) of a robotic manipulator to perform multiple prioritized tasks (Khatib, 1987). Projecting the input required to complete lower priority tasks into the null-space of higher priority tasks ensures that lower-priority tasks do not disturb the higher priority tasks. For torque-controlled robots, using dynamically consistent null-space projections makes it possible to decouple the tasks inertially (Ott et al., 2015). The resulting decoupling is similar to the one achieved by Garofalo et al. (2015), but the use of null-space projections enables the decoupling of the dynamics of an arbitrary choice of tasks, and has been used for both compliant control (Ott et al., 2015) and tracking of time-varying task trajectories (Dietrich and Ott, 2020; Sæbø et al., 2022).

In the previous work applying the GJM to control an AIAUV, Amundsen et al. (2018) consider only joint motion within what effectively becomes a stationary workspace, since thrusters are not used. On the other hand, in previous works such as Sæbø et al. (2022) and Dyrhaug et al. (2023), where both thrusters and joints are utilized to have an AIAUV perform multiple tasks, the allocation of control inputs between thrusters or joint torques has not received much attention. Autonomous underwater vehicles (AUVs), including the AIAUV, are typically actuated by propeller-based thrusters, which are subject to complex dynamics, especially during maneuvers with unsteady flow over the propellers (Healey et al., 1995). In addition, these dynamics are often not included in the models used for control development, resulting in unmodeled input delays and uncertainties. Therefore, it would be beneficial to use thrusters only for gross motion to reposition the workspace of a UVMS, while the joints are used for precise motions during inspection and intervention tasks. In addition, choosing the CG as the point to reposition reduces the need for using thrusters to counteract disturbances from the joint motion, which may contribute to reducing energy consumption and extend mission duration.

In this paper, we demonstrate that the GJM coincides with a dynamically consistent coordinate transformation for prioritized tasks for a particular choice of tasks. This paves the way for extending methods such as those of Giordano et al. (2018) to an arbitrary number of tasks and tasks requiring tracking of time-varying trajectories, and we show that this can be done without losing the beneficial division of actuator use in which thrusters are engaged only for repositioning the overall VMS. We prove that the controller renders the set in which all tracking error are zero uniformly asymptotically stable, also for control objectives in which parts of the system state is left free. Finally, we present a thrust allocation algorithm which ensures that this desirable division of actuator use is achieved also for free-floating VMSs equipped with thrusters on multiple links, such as the AIAUV. This enables the AIAUV to function like a VMS where thrusters are used for gross motion of the workspace, while joints are used for more precise motion within the current workspace. The resulting control scheme is a generalization of the work by Giordano et al. (2018) to time-varying references, an arbitrary number and choice of secondary control objectives, and VMSs with actuators mounted on multiple links.

The paper is organised as follows: the dynamic model of the VMS is presented in Section 2. In Section 3 we introduce the coordinate change to task coordinates, show its relation to the GJM, and examine the structure of the mapping between task coordinates and the original system coordinates. In Section 4 we present the tracking control law and control allocation algorithm, and simulation results are shown in Section 5. Finally, concluding remarks are given in Section 6.

2. VEHICLE MODEL

We consider a UVMS with n revolute joints, resulting in a total of $6 + n$ DOFs. The pose of a frame fixed to the base of the vehicle is given by $\boldsymbol{\eta} = [\boldsymbol{p}^\top \ \boldsymbol{q}^\top]^\top \in \mathbb{R}^3 \times \mathbb{S}^3$, where $\boldsymbol{p}$ is the position of the origin of the base frame, and $\boldsymbol{q}$ is a quaternion representing its attitude relative to an inertial frame. The full configuration of the system is given by $\boldsymbol{\xi} = [\boldsymbol{\eta}^\top\ \boldsymbol{\theta}^\top]^\top \in \mathbb{R}^3 \times \mathbb{S}^3 \times \mathbb{T}^n$, where $\boldsymbol{\theta}$ are the joint angles and $\mathbb{T}^n = \mathbb{S}^1 \times \mathbb{S}^1 \times ... \times \mathbb{S}^1$ is the n-torus. The system velocities are given by $\boldsymbol{\zeta} = [\boldsymbol{\nu}^\top\ \dot{\boldsymbol{\theta}}^\top]^\top \in \mathbb{R}^{6+n}$, which contains the body-fixed base velocities $\boldsymbol{\nu} \in \mathbb{R}^6$ and the joint velocities $\dot{\boldsymbol{\theta}}$. The equations of motion are (From et al., 2014; Schmidt-Didlaukies et al., 2018):

$$\dot{\boldsymbol{\xi}} = \boldsymbol{T}(\boldsymbol{\xi})\boldsymbol{\zeta} \tag{1a}$$

$$\boldsymbol{M}(\boldsymbol{\theta})\dot{\boldsymbol{\zeta}} + \boldsymbol{C}(\boldsymbol{\theta},\boldsymbol{\zeta})\boldsymbol{\zeta} + \boldsymbol{D}(\boldsymbol{\theta},\boldsymbol{\zeta})\boldsymbol{\zeta} + \boldsymbol{g}(\boldsymbol{\eta}) = \boldsymbol{B}(\boldsymbol{\theta})\boldsymbol{u} \tag{1b}$$

where $\boldsymbol{T}(\boldsymbol{\xi})$ is a transformation matrix mapping the body-fixed velocities to the rate of change of the configuration. The matrix $\boldsymbol{M}(\boldsymbol{\theta})$ is the inertia matrix, $\boldsymbol{C}(\boldsymbol{\theta},\boldsymbol{\zeta})\boldsymbol{\zeta}$ is the Coriolis and centripetal matrix, $\boldsymbol{D}(\boldsymbol{\theta},\boldsymbol{\zeta})$ is the hydrodynamic damping matrix and $\boldsymbol{g}(\boldsymbol{\eta})$ is the vector of hydrostatic restoring forces. The matrix $\boldsymbol{B}(\boldsymbol{\theta})$ describes the mapping from the input $\boldsymbol{u} = \left[\boldsymbol{\tau}_{\text{thr}}^\top,\ \boldsymbol{\tau}_\theta^\top\right]^\top$ containing the thruster forces $\boldsymbol{\tau}_{\text{thr}} \in \mathbb{R}^m$ from m thrusters placed on the links of the vehicle, and the joint torques $\boldsymbol{\tau}_\theta \in \mathbb{R}^n$. The model can be parametrised such that the inertia and damping matrices, $\boldsymbol{M}(\boldsymbol{\theta})$ and $\boldsymbol{D}(\boldsymbol{\theta},\boldsymbol{\zeta})\boldsymbol{\zeta}$, are positive definite for all $\boldsymbol{\theta}$, $\boldsymbol{\zeta}$, and $\dot{\boldsymbol{M}}(\boldsymbol{\theta}) - 2\boldsymbol{C}(\boldsymbol{\theta},\boldsymbol{\zeta})$ is skew-symmetric (Antonelli, 2018). The inertia matrix $\boldsymbol{M}(\boldsymbol{\theta})$ can be partitioned as

$$\boldsymbol{M}(\boldsymbol{\theta}) = \begin{bmatrix} \boldsymbol{M}_b(\boldsymbol{\theta}) & \boldsymbol{M}_{bm}(\boldsymbol{\theta}) \\ \boldsymbol{M}_{bm}(\boldsymbol{\theta})^\top & \boldsymbol{M}_m(\boldsymbol{\theta}) \end{bmatrix} \tag{2}$$

where $\boldsymbol{M}_b(\boldsymbol{\theta}) \in \mathbb{R}^{6\times 6}$, $\boldsymbol{M}_{bm}(\boldsymbol{\theta}) \in \mathbb{R}^{6\times n}$, and $\boldsymbol{M}_m(\boldsymbol{\theta}) \in \mathbb{R}^{n\times n}$. The actuator configuration matrix $\boldsymbol{B}(\boldsymbol{\theta})$ can be written as

$$\boldsymbol{B}(\boldsymbol{\theta}) = \begin{bmatrix} \boldsymbol{B}_{\text{thr}}(\boldsymbol{\theta}) & \boldsymbol{0}_{6\times n} \\ \boldsymbol{B}_\theta(\boldsymbol{\theta}) & \boldsymbol{I}_n \end{bmatrix} \tag{3}$$

where $\boldsymbol{B}_{\text{thr}}(\boldsymbol{\theta}) \in \mathbb{R}^{6\times m}$.

Assumption 1. The vehicle is fully actuated at all times, i.e. $\text{rank}(\boldsymbol{B}_{\text{thr}}(\boldsymbol{\theta})) = 6\ \forall \boldsymbol{\theta}$.

Remark 1. Assumption 1 is an assumption that the UVMS is well designed, i.e. equipped with a sufficient number of actuators to ensure controllability of the base motion in any configuration of the UVMS.

Remark 2. For a UVMS with all thrusters placed on the base, $\boldsymbol{B}_\theta(\boldsymbol{\theta}) = 0\ \forall \boldsymbol{\theta}$.

3. DYNAMICALLY CONSISTENT TASK COORDINATES

In this section, we introduce the transformation to task coordinates presented by Dietrich and Ott (2020), and show that the GJM can be derived as the projected Jacobian of an end-effector pose task when the primary task belongs to a family of momentum-like tasks. Finally, we show that the desired structure of the coordinate transformation matrix is preserved for any choice of lower-priority tasks.

3.1 Task coordinate transformation

A task hierarchy comprised of $q \in \mathbb{N}$ tasks is considered, where each task $i = 1, ..., q$ is defined in task-space coordinates as

$$\boldsymbol{x}_i = \boldsymbol{f}_i(\boldsymbol{\xi}) \tag{4}$$

of dimension m_i. As in Dietrich and Ott (2020), the choice of tasks is subject to the following assumptions:

Assumption 2. The tasks are simultaneously feasible and the total dimension of the tasks is equal to the number of DOFs of the system s.t. $\sum_{i=1}^q m_i = 6 + n$.

For each task, the objective is to follow a given desired trajectory $\boldsymbol{x}_{i,d}(t)$, which we gather into $\boldsymbol{x}_d(t) = [\boldsymbol{x}_{1,d}(t)^\top, ..., \boldsymbol{x}_{q,d}(t)^\top]^\top$.

Assumption 3. The desired trajectory $\boldsymbol{x}_d(t)$ avoids any singularities, and there exists an open neighborhood around the desired trajectory in the state space which is also free of singularities.

Assumptions 2 and 3 ensure that the augmented Jacobian for the full stack of tasks is invertible in a neighbourhood of the desired trajectory, which is necessary to realize the control input to be introduced later, and for the later stability analysis to be valid.

The task-space velocities are given by

$$\dot{\boldsymbol{x}}_i = \boldsymbol{J}_i(\boldsymbol{\xi})\boldsymbol{\zeta} \tag{5}$$

where the task Jacobian matrices $\boldsymbol{J}_i(\boldsymbol{\xi}) \in \mathbb{R}^{m_i\times(6+n)}$ are given by

$$\boldsymbol{J}_i(\boldsymbol{\xi}) = \frac{\partial \boldsymbol{f}_i(\boldsymbol{\xi})}{\partial \boldsymbol{\xi}}\boldsymbol{T}(\boldsymbol{\xi}). \tag{6}$$

Stacking the Jacobian matrices gives the augmented Jacobian matrices $\boldsymbol{J}_i^{\text{aug}}(\boldsymbol{\xi}) = \left[\boldsymbol{J}_1^\top\ ...\ \boldsymbol{J}_i^\top\right]^\top$ and corresponding augmented task-space velocities

$$\dot{\boldsymbol{x}}_i^{\text{aug}} = \boldsymbol{J}_i^{\text{aug}}(\boldsymbol{\xi})\boldsymbol{\zeta} \tag{7}$$

with $\dot{\boldsymbol{x}}_i^{\text{aug}} = \left[\dot{\boldsymbol{x}}_1^\top,\ ...,\ \dot{\boldsymbol{x}}_i^\top\right]^\top$. To enforce the strict priority within the task hierarchy and avoid lower-level tasks interfering with ones of higher priority, new prioritized Jacobian matrices are found using dynamically consistent null-space projectors:

$$\bar{\boldsymbol{J}}_i(\boldsymbol{\xi}) = \boldsymbol{J}_i(\boldsymbol{\xi})\boldsymbol{N}_i(\boldsymbol{\xi})^\top \tag{8}$$

where the null-space projectors $\boldsymbol{N}_i(\boldsymbol{\xi}) \in \mathbb{R}^{(6+n)\times(6+n)}$ can be found recursively as in Wu et al. (2022):

$$\boldsymbol{N}_i = \begin{cases} \boldsymbol{I}_{6+n} & \text{for } i = 1, \\ \boldsymbol{N}_{i-1} - \bar{\boldsymbol{J}}_{i-1}^\top \bar{\boldsymbol{J}}_{i-1}^{M+,\top} & \text{for } i = 2, ..., q \end{cases} \tag{9}$$

where ${}^{M+}$ denotes the dynamically consistent pseudoinverse. Since $\boldsymbol{N}_{i-1}$ is a projection matrix, it has to satisfy $\boldsymbol{N}_{i-1} = \boldsymbol{N}_{i-1}^2$, and we can write (9) for $i = 2, ..., q$ as

$$\boldsymbol{N}_i = \boldsymbol{N}_{i-1}\left(\boldsymbol{I}_{6+n} - \bar{\boldsymbol{J}}_{i-1}^\top \bar{\boldsymbol{J}}_{i-1}^{M+,\top}\right). \tag{10}$$

The prioritized Jacobians can be used to find the dynamically consistent task-space velocities $\boldsymbol{v}_i = \bar{\boldsymbol{J}}_i\boldsymbol{\zeta}$. These can be gathered into $\boldsymbol{v} = \left[\boldsymbol{v}_1^\top, ..., \boldsymbol{v}_q^\top\right]^\top$ and written as

$$\boldsymbol{v} = \bar{\boldsymbol{J}}\boldsymbol{\zeta} \tag{11}$$

where $\bar{\boldsymbol{J}} = \left[\bar{\boldsymbol{J}}_1^\top\ ...\ \bar{\boldsymbol{J}}_q^\top\right]^\top$. Assumptions 2 and 3 ensure that $\bar{\boldsymbol{J}}$ is nonsingular, and $\bar{\boldsymbol{J}}^{-1}$ can be expressed as (Wu et al., 2022)

$$\bar{\boldsymbol{J}}^{-1} = \left[\bar{\boldsymbol{J}}_1^{M+}\ ...\ \bar{\boldsymbol{J}}_q^{M+}\right]. \tag{12}$$

Using (11), the VMS dynamics (1b) can be transformed into task-space coordinates:

$$\underbrace{\bar{\boldsymbol{J}}^{-\top}\boldsymbol{M}\bar{\boldsymbol{J}}^{-1}}_{=\bar{\boldsymbol{M}}}\dot{\boldsymbol{v}} + \underbrace{\bar{\boldsymbol{J}}^{-\top}\left(\boldsymbol{C} - \boldsymbol{M}\bar{\boldsymbol{J}}^{-1}\dot{\bar{\boldsymbol{J}}}\right)\bar{\boldsymbol{J}}^{-1}}_{=\boldsymbol{\mu}}\boldsymbol{v} + \underbrace{\bar{\boldsymbol{J}}^{-\top}\boldsymbol{D}\bar{\boldsymbol{J}}^{-1}}_{=\boldsymbol{\delta}}\boldsymbol{v} = \bar{\boldsymbol{J}}^{-\top}\left(\boldsymbol{B}(\boldsymbol{\theta})\boldsymbol{u} - \boldsymbol{g}\right). \tag{13}$$

The transformed inertia matrix $\bar{\boldsymbol{M}}$ is block-diagonal, with blocks $\bar{\boldsymbol{M}}_i \in \mathbb{R}^{m_i\times m_i}$. However, the Coriolis and damping matrices $\boldsymbol{\mu}$ and $\boldsymbol{\delta}$ are in not general block-diagonal, and therefore introduce couplings between the task dynamics to be addressed when designing the control law.

The new, dynamically consistent task velocities are related to the original task-space velocities through

$$\boldsymbol{v} = \underbrace{\bar{\boldsymbol{J}}(\boldsymbol{\xi})\boldsymbol{J}_q^{\text{aug}}(\boldsymbol{\xi})^{-1}}_{=\boldsymbol{G}(\boldsymbol{\xi})}\dot{\boldsymbol{x}}_q^{\text{aug}}. \tag{14}$$

By Assumptions 2 and 3, $\boldsymbol{J}_q^{\text{aug}}$ is invertible in a neighbourhood of the desired task trajectories. The matrix

$\boldsymbol{G}(\boldsymbol{\xi})$ is lower triangular, and can be split into submatrices $\boldsymbol{G}_{i,j} \in \mathbb{R}^{m_i \times m_j}$. These have the properties that $\boldsymbol{G}_{i,j} = \boldsymbol{I}_{m_i}$ for $i = j$, and $\boldsymbol{G}_{i,j} = \boldsymbol{0}$ for $i < j$, yielding

$$\boldsymbol{v}_i = \dot{\boldsymbol{x}}_i + \sum_{j=1}^{i-1} \boldsymbol{G}_{i,j} \dot{\boldsymbol{x}}_j \tag{15}$$

3.2 Relation with the GJM and general structure with momentum as primary task

In this section we derive the GJM as a prioritized Jacobian for a particular choice of tasks, and we show that the beneficial structure of the task and actuator mappings obtained by Giordano et al. (2018) can be preserved when performing tasks other than control of end-effector pose.

Let $\boldsymbol{h} \in \mathbb{R}^6$ be the total momentum about a frame c with origin at the CG of the VMS and a fixed orientation relative to the inertial frame, and given as (Giordano et al., 2018)

$$\boldsymbol{h} = \boldsymbol{Ad}_{cb}^{-\top} \left[\boldsymbol{M}_b \ \boldsymbol{M}_{bm}\right] \boldsymbol{\zeta} \tag{16}$$

where $\boldsymbol{Ad}_{cb}$ denotes the adjoint of the transformation describing the pose of the base frame given in the c-frame. Now let the primary task to be performed have a task velocity which can be written as

$$\boldsymbol{v}_1 = \boldsymbol{X}(\boldsymbol{\xi}) \boldsymbol{h} \tag{17}$$

where $\boldsymbol{X}(\boldsymbol{\xi}) \in \mathbb{R}^{6 \times 6}$ is invertible in the considered workspace. We will refer to tasks with velocity as given by (17) as momentum-like.

Remark 3. Such tasks include the velocity of the CG together with rotational momentum as in Giordano et al. (2018), or a generalized average velocity.

By inserting (16) into (17) we obtain

$$\boldsymbol{v}_1 = \boldsymbol{X} \boldsymbol{Ad}_{cb}^{-\top} \left[\boldsymbol{M}_b \ \boldsymbol{M}_{bm}\right] \boldsymbol{\zeta} = \boldsymbol{J}_1 \boldsymbol{\zeta}. \tag{18}$$

We can then find

$$\boldsymbol{N}_2 = \boldsymbol{I}_{6+n} - \boldsymbol{J}_1^\top \boldsymbol{J}_1^{M+,\top} = \begin{bmatrix} \boldsymbol{0}_{6\times 6} & \boldsymbol{0}_{6\times n} \\ -\boldsymbol{M}_{bm}^\top \boldsymbol{M}_b^{-1} & \boldsymbol{I}_n \end{bmatrix}. \tag{19}$$

It can be verified that $\boldsymbol{N}_2^\top$ is equal to a matrix selecting only the contribution from the joint motion based on the coordinate transformation of Garofalo et al. (2015). Consequently, $\boldsymbol{N}_2^\top$ can be interpreted as a projection into the space of what is called the internal motion of the system by Giordano et al. (2018).

Relation with the GJM Let there be a second task $\boldsymbol{x}_2 \in \mathbb{R}^{m_2}$ whose Jacobian can be split into two parts corresponding to the contributions from base velocity and joint velocities as in Umetani and Yoshida (1989):

$$\dot{\boldsymbol{x}}_2 = \boldsymbol{J}_2 \boldsymbol{\zeta} = \left[\boldsymbol{J}_{2,b} \ \boldsymbol{J}_{2,m}\right] \boldsymbol{\zeta} \tag{20}$$

with $\boldsymbol{J}_{2,b} \in \mathbb{R}^{m_2 \times 6}$, $\boldsymbol{J}_{2,m} \in \mathbb{R}^{m_2 \times n}$. We then have

$$\bar{\boldsymbol{J}}_2 = \boldsymbol{J}_2 \boldsymbol{N}_2^\top = \left[\boldsymbol{0}_{6\times 6} \ \boldsymbol{J}_{2,m} - \boldsymbol{J}_{2,b} \boldsymbol{M}_b^{-1} \boldsymbol{M}_{bm}\right] \tag{21}$$

where $\boldsymbol{J}_{2,m} - \boldsymbol{J}_{2,b} \boldsymbol{M}_b^{-1} \boldsymbol{M}_{bm}^\top$ is the GJM (Umetani and Yoshida, 1989). As a consequence, if the second task is chosen to be the end-effector pose, the dynamically consistent task velocity $\boldsymbol{v}_2$ can be interpreted as the so-called internal end-effector velocity (Giordano et al., 2018).

Triangular structure Looking at the expression (10) for the null-space projectors, it is apparent that every prioritized Jacobian (8) of lower priority tasks, i.e. with $i \geq 2$, will be multiplied by $\boldsymbol{N}_2^\top$. If the primary task belongs to the group of "momentum-like" tasks whose velocity can be described by (17), the expression for $\boldsymbol{N}_2$ given by (19) ensures that the Jacobians $\bar{\boldsymbol{J}}_i$ with $i \geq 2$ all start with six columns of zeros. As a result, $\bar{\boldsymbol{J}}$ has the following block-triangular structure:

$$\bar{\boldsymbol{J}} = \begin{bmatrix} \boldsymbol{X} \boldsymbol{Ad}_{cb}^{-\top} \boldsymbol{M}_b & \boldsymbol{X} \boldsymbol{Ad}_{cb}^{-\top} \boldsymbol{M}_{bm} \\ \boldsymbol{0}_{n\times 6} & \bar{\boldsymbol{J}}_\theta \end{bmatrix} \tag{22}$$

where $\bar{\boldsymbol{J}}_\theta \in \mathbb{R}^{n \times n}$ consists of the last n columns of the Jacobians $\bar{\boldsymbol{J}}_i$, $i = 2, .., q$, stacked. If $\bar{\boldsymbol{J}}$ is invertible, so is $\bar{\boldsymbol{J}}_\theta$. Thus the triangular structure of the coordinate transformation matrix from Giordano et al. (2018) can be achieved for any number and choice of lower-priority tasks when combined with a momentum-like primary task. If the inverse mapping, i.e. the mapping from desired inputs in dynamically consistent task coordinates to the actuators, is correspondingly lower block-triangular, then only the primary task engages the thrusters, while inputs to the lower-priority tasks are realized using only the joints torques. If the input configuration matrix (3) is block-diagonal or lower block-triangular and square, this follows directly when $\bar{\boldsymbol{J}}$ is upper block-triangular. Otherwise, the control allocation must preserve the desired triangular structure of the inverse mapping. This is presented in Subsection 4.2.

4. CONTROL LAW AND CONTROL ALLOCATION

In this section we show how the results of Section 3.2 can be utilized to design a tracking control law and control allocation algorithm which use thrusters only for overall gross motion of the system to reposition its workspace, while the joints are used to perform additional tasks within the workspace. We base our tracking controller on our previous work (Sæbø et al., 2022), with some required modifications, and we analyze the stability of the resulting closed-loop system. Moreover, we present a control allocation algorithm which ensures a triangular structure of the mapping from virtual task inputs to actuators.

As our primary task, like Giordano et al. (2018) we choose to control the position of the CG, denoted $\boldsymbol{p}_{\mathrm{cg}}$, and the total rotational momentum about a frame located at the CG and with axes which are fixed relative to the inertial axes. In order to relate the velocity of the CG to the total momentum in an underwater setting, we make the following assumption in the control design and analysis:

Assumption 4. The added mass effects are negligible.

Remark 4. The presence of added mass effects will result in a disturbance which is not compensated directly by the controller, nor taken into account in the analysis. Since knowledge of the added mass effects will be approximate at best, and unnecessarily complicate the notion of controlling the center of mass, we let this disturbance be dealt with by the general robustness of the controller. This will be further discussed in connection with simulation results in Section 5.

The task velocity $\boldsymbol{v}_1 = \left[\dot{\boldsymbol{p}}_{\mathrm{cg}}^\top, \boldsymbol{h}_{\mathrm{rot}}\right]^\top$, where $\boldsymbol{h}_{\mathrm{rot}}$ is the rotational momentum, is then given by (17) with

$$\boldsymbol{X} = \begin{bmatrix} \frac{1}{m_{\mathrm{tot}}} \boldsymbol{I}_3 & \boldsymbol{0}_{3\times 3} \\ \boldsymbol{0}_{3\times 3} & \boldsymbol{I}_3 \end{bmatrix} \tag{23}$$

where m_{tot} is the total mass of the VMS. The references for the position of the CG and lower-priority tasks are in general considered to be time-varying, while for the momentum the goal is to drive it to zero. Thus we have no task variable $\boldsymbol{x}_1$ such that $\dot{\boldsymbol{x}}_1 = \boldsymbol{v}_1$. Instead we describe the primary task using only $\boldsymbol{p}_{\mathrm{cg}}$ and $\boldsymbol{v}_1$. We then have $q-1$ additional tasks of the form described in Subsection 3.1.

4.1 Tracking control law

For the tracking control, we will apply the tracking controller from our previous work, Sæbø et al. (2022), with some modifications required to adapt it to our choice of primary task. Let

$$\bar{\boldsymbol{J}}^{-\top}\boldsymbol{B}(\boldsymbol{\theta})\boldsymbol{u} = \boldsymbol{F} \tag{24}$$

where we treat $\boldsymbol{F}$ as a virtual input to the dynamically consistent task velocities. The control allocation problem of finding the corresponding control inputs $\boldsymbol{u}$ will be solved later in Section 4.2. We select

$$\boldsymbol{F} = \bar{\boldsymbol{J}}^{-\top}\boldsymbol{g} + \boldsymbol{F}_\mu^* + \boldsymbol{F}_\delta + \begin{bmatrix} \boldsymbol{F}_{1,\mathrm{ctrl}} \\ \vdots \\ \boldsymbol{F}_{q,\mathrm{ctrl}} \end{bmatrix} \tag{25}$$

where $\boldsymbol{F}_{i,\mathrm{ctrl}}$ is a control input for task i. Furthermore, we have

$$\boldsymbol{F}_\delta = \sum_{i=1}^{q}\left(\sum_{j=1}^{i-1}\boldsymbol{\delta}_{i,j}\boldsymbol{v}_j + \sum_{j=i+1}^{q}\boldsymbol{\delta}_{i,j}\boldsymbol{v}_j\right) \tag{26}$$

and

$$\boldsymbol{F}_\mu^* = \sum_{i=2}^{q}\left(\sum_{j=1}^{i-1}\boldsymbol{\mu}_{i,j}\boldsymbol{v}_j + \sum_{j=i+1}^{q}\boldsymbol{\mu}_{i,j}\boldsymbol{v}_j\right), \tag{27}$$

where $\boldsymbol{\mu}_{i,j}$, $\boldsymbol{\delta}_{i,j} \in \mathbb{R}^{m_i\times m_j}$ denote blocks of the matrices $\boldsymbol{\mu}$, $\boldsymbol{\delta}$ from (13).

In Sæbø et al. (2022), we considered vehicles which are actuated directly by a generalized force $\boldsymbol{\tau}$, and the control law (25) is equivalent to the one from Sæbø et al. (2022) with $\boldsymbol{\tau} = \bar{\boldsymbol{J}}^\top\boldsymbol{F}$, except for the term $\boldsymbol{F}_\mu^*$. For $\boldsymbol{X}$ constant, and following along the same reasoning as Garofalo et al. (2015), namely that momentum is conserved in the absence of external forces, it can be shown that the first 6 rows of the term $\boldsymbol{\mu}\boldsymbol{v}$ are equal to 0 in (13). Thus no cancellation of these terms for the first task is necessary. Changing the summation in (27) to go over all $i = 1, ..., q$ (equivalently to (26) for $\boldsymbol{F}_\delta$) recovers the control law presented by Sæbø et al. (2022).

Inserting (25) into (13) fully decouples the dynamics of the dynamically consistent task-velocities, and the resulting dynamics of each task $i = 1, ..., q$ are now

$$\bar{\boldsymbol{M}}_i\dot{\boldsymbol{v}}_i + (\boldsymbol{\mu}_{i,i} + \boldsymbol{\delta}_{i,i})\,\boldsymbol{v}_i = \boldsymbol{F}_{i,\mathrm{ctrl}}. \tag{28}$$

For the lower-priority tasks with $i \geq 2$, these dynamics can be transformed back into the original task coordinates by differentiating (15) and inserting for $\boldsymbol{v}_i$, $\dot{\boldsymbol{v}}_i$, resulting in

$$\bar{\boldsymbol{M}}_i\ddot{\boldsymbol{x}}_i + (\boldsymbol{\mu}_{i,i} + \boldsymbol{\delta}_{i,i})\,\dot{\boldsymbol{x}}_i + \boldsymbol{\gamma}_i\begin{bmatrix}\dot{\boldsymbol{x}}_i^{\mathrm{aug}} \\ \ddot{\boldsymbol{x}}_i^{\mathrm{aug}}\end{bmatrix} = \boldsymbol{F}_{i,\mathrm{ctrl}} \tag{29}$$

where

$$\boldsymbol{\gamma}_i(\boldsymbol{\xi}, \dot{\boldsymbol{\xi}}) = [\boldsymbol{\Gamma}_{i,1}, ..., \boldsymbol{\Gamma}_{i,i-1}, \boldsymbol{\Psi}_{i,1}, ..., \boldsymbol{\Psi}_{i,i-1}] \tag{30a}$$

$$\boldsymbol{\Gamma}_{i,j} = (\boldsymbol{\mu}_{i,i} + \boldsymbol{\delta}_{i,i})\,\boldsymbol{G}_{i,j} + \bar{\boldsymbol{M}}_i\dot{\boldsymbol{G}}_{i,j},\ \boldsymbol{\Psi}_{i,j} = \bar{\boldsymbol{M}}_i\boldsymbol{G}_{i,j}. \tag{30b}$$

The general form of the virtual control inputs $\boldsymbol{F}_{i,\mathrm{ctrl}}$, which we will apply to the lower priority tasks with $i \geq 2$, is given by Sæbø et al. (2022) as

$$\begin{aligned}\boldsymbol{F}_{i,\mathrm{ctrl}} = \bar{\boldsymbol{M}}_i\ddot{\boldsymbol{x}}_{i,r} &+ (\boldsymbol{\mu}_{i,i} + \boldsymbol{\delta}_{i,i})\,\dot{\boldsymbol{x}}_{i,r} \\ &- \boldsymbol{D}_i\boldsymbol{s}_i - \boldsymbol{K}_i\tilde{\boldsymbol{x}}_i + \boldsymbol{\gamma}_i\begin{bmatrix}\dot{\boldsymbol{x}}_{i-1,d}^{\mathrm{aug}} \\ \ddot{\boldsymbol{x}}_{i-1,d}^{\mathrm{aug}}\end{bmatrix}\end{aligned} \tag{31}$$

where $\tilde{\boldsymbol{x}}_i = \boldsymbol{x}_i - \boldsymbol{x}_{i,d}(t)$ are the task tracking errors, and

$$\dot{\boldsymbol{x}}_{i,r} = \dot{\boldsymbol{x}}_{i,d} - \boldsymbol{\Lambda}_i\tilde{\boldsymbol{x}}_i \tag{32}$$

$$\boldsymbol{s}_i = \dot{\tilde{\boldsymbol{x}}}_i + \boldsymbol{\Lambda}_i\tilde{\boldsymbol{x}}_i = \dot{\boldsymbol{x}}_i - \dot{\boldsymbol{x}}_{i,r}. \tag{33}$$

The matrices $\boldsymbol{\Lambda}_i$, $\boldsymbol{K}_i$, $\boldsymbol{D}_i$ are control gain matrices and must be chosen positive definite.

Control input for the CG and momentum task For the primary task, we choose

$$\begin{aligned}\boldsymbol{F}_{1,\mathrm{ctrl}} = \bar{\boldsymbol{M}}_1\begin{bmatrix}\ddot{\boldsymbol{p}}_{\mathrm{cg},r} \\ \boldsymbol{0}\end{bmatrix} &+ (\boldsymbol{\mu}_{1,1} + \boldsymbol{\delta}_{1,1})\begin{bmatrix}\dot{\boldsymbol{p}}_{\mathrm{cg},r} \\ \boldsymbol{0}\end{bmatrix} \\ &+ \begin{bmatrix}-\boldsymbol{D}_{1,p}\,(\dot{\boldsymbol{p}}_{\mathrm{cg}} - \dot{\boldsymbol{p}}_{\mathrm{cg},r}) - \boldsymbol{K}_{1,p}\tilde{\boldsymbol{p}}_{\mathrm{cg}} \\ -\boldsymbol{D}_{1,h}\boldsymbol{h}_{\mathrm{rot}}\end{bmatrix}\end{aligned} \tag{34}$$

where

$$\dot{\boldsymbol{p}}_{\mathrm{cg},r} = \dot{\boldsymbol{p}}_{\mathrm{cg},d} - \boldsymbol{\Lambda}_{1,p}\tilde{\boldsymbol{p}}_{\mathrm{cg}} \tag{35}$$

and $\boldsymbol{\Lambda}_{1,p}$, $\boldsymbol{K}_{1,p}$, $\boldsymbol{D}_{1,p}$, $\boldsymbol{D}_{1,h}$ are positive definite gain matrices. The choice (34) corresponds to (31) with $\boldsymbol{h}_{\mathrm{rot},d} = 0$ s.t. the last three elements of $\boldsymbol{s}_1$ are equal to $\boldsymbol{h}_{\mathrm{rot}}$, and inserting $[\tilde{\boldsymbol{p}}_{\mathrm{cg}}^\top, \boldsymbol{0}^\top]^\top$ in place of $\tilde{\boldsymbol{x}}_1$. When added mass effects are neglected in the mass matrix $\boldsymbol{M}$ as stated in Assumption 4, the task inertia $\bar{\boldsymbol{M}}_1$ for this primary task becomes block-diagonal as in Giordano et al. (2018), and the upper left 3×3 block of $\boldsymbol{\mu}_{1,1}$ consists of zeros.

Remark 5. If the reference for the position of CG is also chosen constant, and in the absence of external damping or hydrostatic forces, the control law given by (25), (31) for the momentum task reduces to the same one as in (Giordano et al., 2018) with total proportional gain $\boldsymbol{D}_{1,p}\boldsymbol{\Lambda}_{1,p} + \boldsymbol{K}_{1,p}$. If the lower-priority tasks are chosen to be only the regulation of end-effector pose as in the scenario considered by Giordano et al. (2018), the complete input (25), (31) for the end-effector task differs only by the cancellation of Coriolis terms through $\boldsymbol{F}_\mu^*$.

4.2 Control allocation

To ensure that thrusters are used for gross motion of the workspace, while joints are used for more precise motion within the current workspace, the control allocation must be designed to preserve the desired triangular structure when inverting the mapping (25) in order to map the virtual inputs $\boldsymbol{F}$ to actuator inputs $\boldsymbol{u}$. When the matrix $\boldsymbol{B}(\boldsymbol{\theta})$ given by (3) is lower block-triangular, and when $\bar{\boldsymbol{J}}$ has the form (22), the product $\bar{\boldsymbol{J}}^{-\top}(\boldsymbol{\xi})\boldsymbol{B}(\boldsymbol{\theta})$ is likewise lower block triangular. As a consequence, joint torques have no impact on the primary task as intended. In order to also ensure that thrusters are engaged only to realize the input to the primary task, the inverse of the mapping $\bar{\boldsymbol{J}}^{-\top}(\boldsymbol{\xi})\boldsymbol{B}(\boldsymbol{\theta})$ must also be lower block-triangular. However, the pseudoinverse of a block-triangular matrix is not necessarily block-triangular (Meyer, 1970).

Based on Meyer (1970), for a block-triangular matrix $\boldsymbol{A} = \left[\begin{smallmatrix}\boldsymbol{A}_{11} & 0 \\ \boldsymbol{A}_{21} & \boldsymbol{A}_{22}\end{smallmatrix}\right]$, we define

$$\boldsymbol{A}^\ddagger \triangleq \begin{bmatrix}\boldsymbol{A}_{11}^\dagger & \boldsymbol{0} \\ -\boldsymbol{A}_{22}^\dagger\boldsymbol{A}_{21}\boldsymbol{A}_{11}^\dagger & \boldsymbol{A}_{22}^\dagger\end{bmatrix} \tag{36}$$

The matrix $\boldsymbol{A}^\ddagger$ is a so-called (1,2,3)-pseudoinverse of $\boldsymbol{A}$ if (and only if) the range of the matrix $\boldsymbol{A}_{21}$ is a subset of the range of $\boldsymbol{A}_{22}$ (Meyer, 1970). If $\boldsymbol{A}_{22}$ is square and has full rank, this condition is satisfied trivially. If, in addition, the range of $\boldsymbol{A}_{21}^\top$ is a subset of the range of $\boldsymbol{A}_{11}^\top$, then $\boldsymbol{A}^\ddagger = \boldsymbol{A}^\dagger$.

We solve (24) for $\boldsymbol{u}$ by allocating the control inputs according to

$$\boldsymbol{u} = \left(\bar{\boldsymbol{J}}^{-\top}\boldsymbol{B}(\boldsymbol{\theta})\right)^\ddagger\boldsymbol{F}. \tag{37}$$

By Assumption 1, $\boldsymbol{B}_{\mathrm{thr}}$ has full row rank so that we have $\boldsymbol{B}_{\mathrm{thr}}\boldsymbol{B}_{\mathrm{thr}}^\dagger = \boldsymbol{I}_6$. When, as a consequence of Assumption 3, $\bar{\boldsymbol{J}}$ also has full rank, it can be shown that

$$\left(\bar{\boldsymbol{J}}^{-\top}\boldsymbol{B}(\boldsymbol{\theta})\right)^\ddagger = \boldsymbol{B}(\boldsymbol{\theta})^\ddagger\bar{\boldsymbol{J}}^\top. \tag{38}$$

Using this and inserting (25) for $\boldsymbol{F}$ into (37), we can avoid transforming $\boldsymbol{g}$ back and forth between original and task coordinates.

Remark 6. This control allocation scheme effectively requires the joints to counter the torques exerted on them by the thrusters, and therefore relies on the joint motors being powerful enough to achieve that.

4.3 Stability analysis

Since there is no task error associated with the task velocity $\boldsymbol{h}_{\text{rot}}$, the completion of all tasks does not uniquely specify the system state. Let $\boldsymbol{s}_1 = \left[(\dot{\boldsymbol{p}}_{\text{cg}} - \dot{\boldsymbol{p}}_{\text{cg},r})^\top, \boldsymbol{h}_{\text{rot}}^\top\right]^\top$ and $\boldsymbol{s} = \left[\boldsymbol{s}_1^\top, ..., \boldsymbol{s}_q^\top\right]^\top$. Let the full state of the system be described by $\boldsymbol{z} = [\tilde{\boldsymbol{p}}_{\text{cg}}^\top, \boldsymbol{q}^\top, \boldsymbol{\theta}^\top, \boldsymbol{s}^\top]^\top$, and let the complete state space be denoted $\mathcal{A}_0$. Similarly to Dietrich and Ott (2020), we define successive nested sets in which consecutive tasks are completed, the first of which we define as

$$\mathcal{A}_1 = \left\{\boldsymbol{z} \,|\, \tilde{\boldsymbol{p}}_{\text{cg}} = 0,\, \dot{\tilde{\boldsymbol{p}}}_{\text{cg}} = 0,\, \boldsymbol{h}_{\text{rot}} = 0\right\} \tag{39}$$

which is the subset of the state space in which the first task is completed. We then define the nested subsets

$$\mathcal{A}_i = \mathcal{A}_{i-1} \cap \{\boldsymbol{z} \,|\, \tilde{\boldsymbol{x}}_i = 0,\, \boldsymbol{s}_i = 0\} \tag{40}$$

for $i = 2, ..., q$. From the expression (33) for $\boldsymbol{s}_i$ it follows that in the set $\mathcal{A}_i$ where $\tilde{\boldsymbol{x}}_i = 0$, $\dot{\tilde{\boldsymbol{x}}}_i = \boldsymbol{s}_i = 0$. Thus $\mathcal{A}_i$ is the subset of the state space in which all tasks up to and including task i are completed. The control objective is then to asymptotically stabilize the set $\mathcal{A}_q$ in which all tasks are completed.

Assumption 5. The dynamics (1) in closed-loop with the control input given by (25), (31), (34), (37) are Lipschitz.

Remark 7. Assumption 5 is necessary in order to apply stability theorems from Maggiore et al. (2023), and is a common assumption (Dietrich and Ott, 2020). It is a reasonable assumption for the robot dynamics (1), but may restrict the choice of tasks.

Proposition 1. Consider the dynamics (1) in closed-loop with the control input given by (25), (31), (34), (37), and subject to Assumptions 1-5. Then the set $\mathcal{A}_q$ is uniformly asymptotically stable (UAS).

Proof. Since the attitude and joint angles $\boldsymbol{q}, \boldsymbol{\theta}$ evolve on compact manifolds, the set $\mathcal{A}_q$ is compact. The closed-loop dynamics of the primary task given by (29), (34), (35) are

$$\bar{\boldsymbol{M}}_1 \dot{\boldsymbol{s}}_1 + (\boldsymbol{\mu}_{1,1} + \boldsymbol{\delta}_{1,1} + \boldsymbol{D}_1)\, \boldsymbol{s}_1 + \begin{bmatrix} \boldsymbol{K}_{1,p}\tilde{\boldsymbol{p}}_{cg,r} \\ \boldsymbol{0} \end{bmatrix} = 0 \tag{41a}$$

$$\dot{\tilde{\boldsymbol{p}}}_{cg} = -\boldsymbol{\Lambda}_i \tilde{\boldsymbol{p}}_{cg} + (\dot{\boldsymbol{p}}_{\text{cg}} - \dot{\boldsymbol{p}}_{\text{cg},r}) \tag{41b}$$

where $\boldsymbol{D}_1$ is block-diagonal with blocks $\boldsymbol{D}_{1,p}$, $\boldsymbol{D}_{1,h}$. Within a set $\mathcal{A}_{i-1}$, with $i \geq 2$, the closed-loop dynamics of task i given by (29), (31), (33) become

$$\bar{\boldsymbol{M}}_i \dot{\boldsymbol{s}}_i + (\boldsymbol{\mu}_{i,i} + \boldsymbol{\delta}_{i,i} + \boldsymbol{D}_i)\, \boldsymbol{s}_i + \boldsymbol{K}_i \tilde{\boldsymbol{x}}_i = 0, \tag{42a}$$

$$\dot{\tilde{\boldsymbol{x}}}_i = -\boldsymbol{\Lambda}_i \tilde{\boldsymbol{x}}_i + \boldsymbol{s}_i. \tag{42b}$$

The analysis follows along similar lines as those of Dietrich and Ott (2020); Sæbø et al. (2022), except $\mathcal{A}_q$ is now a compact set containing more than a single point. Therefore we will apply theorems for stability of compact sets from Maggiore et al. (2023).

By Assumption 3, the trajectories of the system must be compatible, hence there exists an open neighborhood U containing no singularities, with $\mathcal{A}_q \subset U$. Within the set U, the Jacobians $\boldsymbol{J}^{\text{aug}}$, $\bar{\boldsymbol{J}}$ are invertible. At each priority level $i \geq 2$, as in Sæbø et al. (2022) we choose

$$V_i(\tilde{\boldsymbol{x}}_i, \boldsymbol{s}_i, \boldsymbol{\theta}) = \tfrac{1}{2} \boldsymbol{s}_i^\top \bar{\boldsymbol{M}}_i(\boldsymbol{\theta}) \boldsymbol{s}_i + \tilde{\boldsymbol{x}}_i^\top \boldsymbol{K}_i \tilde{\boldsymbol{x}}_i \tag{43}$$

and for task 1

$$V_1(\tilde{\boldsymbol{p}}_{cg}, \boldsymbol{s}_1, \boldsymbol{\theta}) = \tfrac{1}{2} \boldsymbol{s}_1^\top \bar{\boldsymbol{M}}_1(\boldsymbol{\theta}) \boldsymbol{s}_1^\top + \tilde{\boldsymbol{p}}_{cg}^\top \boldsymbol{K}_1 \tilde{\boldsymbol{p}}_{cg}. \tag{44}$$

Let $\boldsymbol{y}_1 = \left[\tilde{\boldsymbol{p}}_{cg}^\top, \boldsymbol{s}_1^\top\right]^\top$, and for for $i = 2, ..., q$, let $\boldsymbol{y}_i = \left[\tilde{x}_i^\top, \boldsymbol{s}_i^\top\right]^\top$. Then for $i = 1, ..., q$ it can be shown the functions V_i (43), (44) satisfy

$$k_{1,i}\|\boldsymbol{y}_i\|^2 \leq V_i \leq k_{2,i}\|\boldsymbol{y}_i\|^2 \tag{45a}$$

$$\dot{V}_i \leq k_{3,i}\|\boldsymbol{y}_i\|^2 \tag{45b}$$

for $\boldsymbol{z} \in \mathcal{A}_{i-1} \cap U$. The rest of the proof follows along these steps:

1) We first establish that $\mathcal{A}_q$ is UAS relative to $\mathcal{A}_{q-1}$.
2) We then establish that $\mathcal{A}_i$ is *locally uniformly stable (LUS) near* $\mathcal{A}_q$ relative to $\mathcal{A}_{i-1}$ for each $i = 1, ..., q-1$, using (Maggiore et al., 2023, Proposition 25).
3) We then apply the following steps for each i, starting with $i = q-1$ and up to $i = 1$:
   3a) Using the fact that $\mathcal{A}_q$ is UAS and thus uniformly stable (US) relative to $\mathcal{A}_i$, we establish the property of t_0*-uniform attractivity of* $\mathcal{A}_i$ *near* $\mathcal{A}_q$ relative to $\mathcal{A}_{i-1}$ using (Maggiore et al., 2023, Corollary 29).
   3b) By applying (Maggiore et al., 2023, Theorem 18), we conclude that $\mathcal{A}_q$ is UAS relative to $\mathcal{A}_{i-1}$.

   Repeating these steps up to $i = 1$, we arrive at the conclusion that $\mathcal{A}_q$ is UAS relative to $\mathcal{A}_0$.

For the definitions of t_0-uniform attractivity and stability properties near a set, we refer the reader to (Maggiore et al., 2023).

Step 1) From the dynamics (42), (41) we can conclude (by inserting $\boldsymbol{y}_i = 0$) that the sets $\mathcal{A}_i$, $i = 1, ..., q$ are positively invariant. Therefore, for initial states $\boldsymbol{z}(t_0) \in \mathcal{A}_{q-1}$ the solutions remain in $\mathcal{A}_{q-1}$. Furthermore, as a consequence of the bounds (45), solutions starting sufficiently close to the set $\mathcal{A}_q$ will remain in U. Then V_q satisfies the bounds (45) along solutions starting in $\mathcal{A}_{q-1}$ and near $\mathcal{A}_q$, and we can apply the comparison lemma (Khalil, 2002, Lemma 3.4) along the same lines as in the proof of (Khalil, 2002, Theorem 4.10) for exponential stability of the origin. We then arrive at

$$\begin{aligned}\|\boldsymbol{z}(t)\|_{\mathcal{A}_q} = \|\boldsymbol{y}_q(t)\| &\leq \sqrt{\tfrac{k_{2,q}}{k_{1,q}}}\|\boldsymbol{y}_q(t_0)\| e^{-\frac{k_{3,q}}{2k_{2,q}}(t-t_0)} \\ &= \sqrt{\tfrac{k_{2,q}}{k_{1,q}}}\|\boldsymbol{z}(t_0)\|_{\mathcal{A}_q} e^{-\frac{k_{3,q}}{2k_{2,q}}(t-t_0)}\end{aligned} \tag{46}$$

where $\|\cdot\|_{\mathcal{A}_q}$ denotes the distance to the set $\mathcal{A}_q$. From (46) and (Maggiore et al., 2023, Definition 12) of relative stability properties, we can conclude that $\mathcal{A}_q$ is UAS relative to $\mathcal{A}_{q-1}$.

Step 2) Within the set $\mathcal{A}_{i-1}$, the function V_i satisfies (45), and from (45a) we have

$$\begin{aligned}k_{1,i}\|\boldsymbol{z}\|_{\mathcal{A}_i}^2 &= k_{1,i}\|\boldsymbol{y}_i\|^2 \leq V_i \\ &\leq k_{2,i}\|\boldsymbol{y}_i\|^2 \leq k_{2,i}\sum_{j=i}^{q}\|\boldsymbol{y}_j\|^2 = k_{2,i}\|\boldsymbol{z}\|_{\mathcal{A}_q}^2\end{aligned} \tag{47}$$

for $\boldsymbol{z} \in \mathcal{A}_{i-1}$, where $\|\cdot\|_{\mathcal{A}_j}$ denotes the distance to $\mathcal{A}_j$. Hence by (Maggiore et al., 2023, Proposition 25), each $\mathcal{A}_i$ is LUS near $\mathcal{A}_q$ relative to $\mathcal{A}_{i-1}$ for $i = 1, ..., q-1$.

Step 3a) Starting with $i = q-1$, $\mathcal{A}_q$ is UAS and thus US relative to $\mathcal{A}_i$. Again, within the set $\mathcal{A}_{i-1}$, the function V_i satisfies (45), and thus by (Maggiore et al., 2023, Corollary 29), we conclude that $\mathcal{A}_i$ is t_0-uniformly attractive (t_0-UA) near $\mathcal{A}_q$ relative to $\mathcal{A}_i$.

Step 3b) Since $\mathcal{A}_q$ is UAS relative to $\mathcal{A}_i$, and $\mathcal{A}_i$ is LUS near $\mathcal{A}_q$ and t_0-UA near $\mathcal{A}_q$, both relative to $\mathcal{A}_{i-1}$, by (Maggiore et al., 2023, Theorem 18) $\mathcal{A}_q$ is UAS relative to $\mathcal{A}_{i-1}$. □

5. SIMULATION RESULTS

The proposed control method is simulated on an AIAUV which has $n = 8$ revolute joints, giving a total of 14 DOF, and is equipped with $m = 9$ thrusters. Fig. 2 illustrates the placement and direction of thrusters and joints. The simulated AIAUV is the same as the robot used by Borlaug et al. (2021), but equipped with two additional thrusters on its center link to ensure that it is always actuated in roll, in order to satisfy Assumption 1. We choose $q = 3$ tasks as follows: the primary task is to control the position of the CG and total rotational momentum, as described in Section 4. As task 2 we choose the pose of the end-effector, with task dimension $m_2 = 6$. Finally as task 3 we choose to point the opposite end, i.e. the base link of the AIAUV, by controlling its pitch and yaw, with task dimension $m_3 = 2$. The control gains are chosen to be $\boldsymbol{\Lambda}_{1,p} = \boldsymbol{K}_{1,p} = \boldsymbol{D}_{1,h} = \boldsymbol{I}_3$, $\boldsymbol{D}_{1,p} = 5\boldsymbol{I}_3$, $\boldsymbol{\Lambda}_2 = \boldsymbol{D}_2 = \boldsymbol{I}_6$, $\boldsymbol{K}_2 = \left[\begin{smallmatrix} 5\boldsymbol{I}_3 & \boldsymbol{0} \\ \boldsymbol{0} & 10\boldsymbol{I}_3 \end{smallmatrix}\right]$, $\boldsymbol{\Lambda}_3 = 0.1\boldsymbol{I}_2$, $\boldsymbol{K}_3 = 7.5\boldsymbol{I}_2$ and $\boldsymbol{D}_3 = 5\boldsymbol{I}_2$. The simulated dynamics include added mass effects, which were not considered in the derivation of the decoupling coordinate transformation. The control input is calculated based only on the rigid body mass, which allows us to test the robustness of the proposed control approach against these effects.

The reference trajectories and the task trajectories are shown in Fig. 3. The joint angles, torques and thruster forces are shown in Fig. 4, and the norms of the tracking errors are shown in Fig. 5. For the second task, the error variables $\tilde{\boldsymbol{x}}_2$, $\boldsymbol{s}_2$ are split into translational and rotational parts before their norms are taken. As can be seen in Figs. 3 and 5, all objectives are tracked well, even when the conditions of Proposition 1 are not fully met, due to the presence of added mass effects. The position of the CG converges to its desired value, after which it remains within less than 1 cm of its reference position despite the significant movement of the end-effector. Fig. 5 shows that all the tracking errors are bounded. The lowest-priority task has the largest error, which is to be expected, as errors in higher-priority tasks give top-down disturbances in the task hierarchy. On the other hand, we see in Fig. 3 that there are some small deviations in the position of the CG from its desired position, despite this being the task with the highest priority. The added mass effects, which were not taken into account in the decoupling coordinate transform in the control input, introduce a disturbance to each individual task, as well as a coupling between the tasks, causing bottom-up disturbances in the task hierarchy. Taking a simplified view of the task interconnections as time-varying signals, the individual task dynamics (42) can be viewed as exponentially stable subsystems subject to a disturbance. In the presence of an additional disturbance, such as caused by added mass effects, higher-priority tasks may not converge entirely to their references and the disturbances will not necessarily vanish. However, the exponential stability of each subsystem provides some robustness against non-vanishing bounded disturbances (Khalil, 2002, Lemma 9.2). In order to further improve performance, a robust control method could be applied, as in e.g. Dyrhaug et al. (2023).

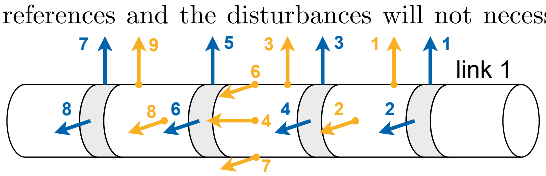

Fig. 2. Illustration of the axes of rotation of joints (blue) and thruster placement and directions (orange) for the simulated AIAUV. The placement of thruster no. 5 mirrors that of no. 4.

The workspace available to the end-effector when using the GJM, i.e. the workspace which is reachable without shifting the CG of the system, is smaller than the workspace reachable by the same manipulator if its base were fixed. In order to reach points in the interior its workspace without shifting the position of the CG, the AIAUV must contract its body using all its joints. This may require large joint angles, as can be seen in Fig. 4. The workspace in which the end-effector can realistically operate is therefore even smaller. The reduced workspace size, when taken together with the requirements posed by Assumptions 2 and 3 that all DOFs must be employed and references must be compatible, requires a thorough planning phase beforehand to ensure the coordination between repositioning the CG and the motion of the end-effector.

Fig. 4 shows that the applied thruster forces and joint torques stay within reasonable values throughout the simulation, demonstrating that the proposed control allocation scheme is feasible. It should be noted however, that even though the motivation for the proposed control method was to reduce the use of thrusters, the thrusters are active at all times. This is due to the cancellation of the hydrodynamic damping terms which would otherwise introduce a coupling between tasks and cause an undesired bottom-up disturbance in the task hierarchy. Cancelling or compensating for this disturbance is necessary in an underwater setting regardless of the choice of tasks. The ability of the control method proposed in this paper to accurately control the position of the CG while performing other tasks shows great promise, and further simulation studies should be performed to compare its performance and required control effort against other choices of tasks.

6. CONCLUSIONS

Moving the CG of a light VMS to reposition its manipulator workspace, rather than the vehicle base, reduces the need to counteract disturbances due to the joint motion. In this paper, a control method was proposed in which the motion of the CG was chosen as the first task in a prioritized task hierarchy comprised of an arbitrary number of additional tracking tasks. A control allocation scheme using a (1,2,3)-pseudoinverse was proposed to ensure that the thrusters are used only for moving the CG, while the joint torques are used to accomplish precise tracking of other task trajectories. The set in which all task tracking errors are zero is shown to be uniformly asymptotically stable, and the proposed control method is shown to work well in simulation. In the future, a more thorough simulation study should be performed, comparing the proposed method and the resulting control effort against that of choosing to control the end-effector and base of the VMS.

REFERENCES

Amundsen, M.F., Sverdrup-Thygeson, J., Kelasidi, E., and Pettersen, K.Y. (2018). Inverse kinematic control of a free-floating underwater manipulator using the generalized Jacobian matrix. In *Proc. 2018 European Control Conf.* Limassol, Cyprus.

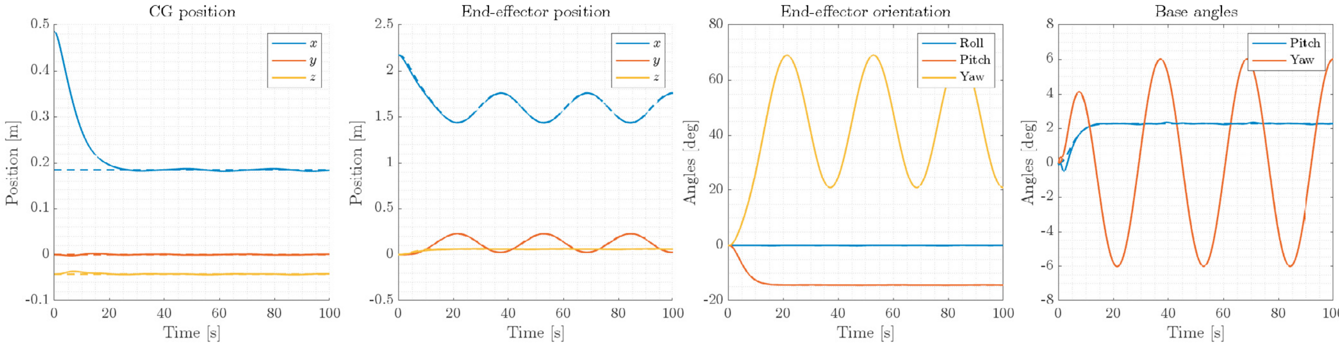

Fig. 3. Task trajectories, with their corresponding reference trajectories as dashed lines

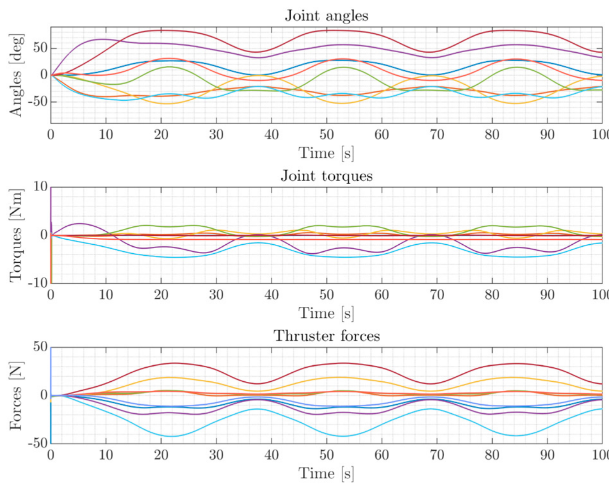

Fig. 4. Joint angles and applied torques and thruster forces

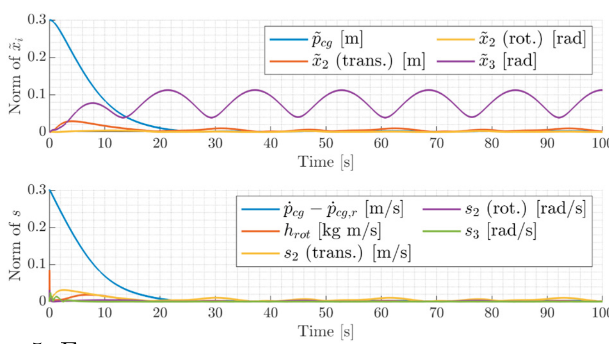

Fig. 5. Error norms

Antonelli, G. (2018). *Underwater Robots.* Springer Int. Publishing, 4th edition.

Borlaug, I.L.G., Pettersen, K.Y., and Gravdahl, J.T. (2021). Tracking control of an articulated intervention autonomous underwater vehicle in 6dof using generalized super-twisting: Theory and experiments. *IEEE Trans. Control Syst. Technol.*, 29(1), 353–369.

Dietrich, A. and Ott, C. (2020). Hierarchical impedance-based tracking control of kinematically redundant robots. *IEEE Trans. Robot.*, 36(1), 204–221.

Dyrhaug, J.I., Tveter, E., Schmidt-Didlaukies, H.M., Basso, E.A., Pettersen, K.Y., and Gravdahl, J.T. (2023). Robust hierarchical tracking control of vehicle-manipulator systems. *IFAC-PapersOnLine*, 56(2), 6696–6702. 22nd IFAC World Congr.

From, P.J., Gravdahl, J.T., and Pettersen, K.Y. (2014). *Vehicle-Manipulator Systems: Modeling for Simulation, Analysis and Control.* Springer-Verlag.

Garofalo, G., Beck, F., and Ott, C. (2018). Task-space tracking control for underactuated aerial manipulators. In *Proc. 2018 European Control Conf.* Limassol, Cyprus.

Garofalo, G., Henze, B., Englsberger, J., and Ott, C. (2015). On the inertially decoupled structure of the floating base robot dynamics. *IFAC-PapersOnLine*, 48(1), 322–327. 8th Vienna Int. Conf. Math. Model.

Giordano, A.M., Calzolari, D., and Albu-Schäffer, A. (2018). Workspace fixation for free-floating space robot operations. In *Proc. 2018 IEEE Int. Conf. Robot. Autom.* Brisbane, Australia.

Giordano, A.M., Garofalo, G., De Stefano, M., Ott, C., and Albu-Schäffer, A. (2016). Dynamics and control of a free-floating space robot in presence of nonzero linear and angular momenta. In *Proc. 2016 IEEE 55th Conf. Decis. Control.* Las Vegas, USA.

Healey, A.J., Rock, S.M., Cody, S., Miles, D., and Brown, J.P. (1995). Toward an improved understanding of thruster dynamics for underwater vehicles. *IEEE J. Ocean. Eng.*, 20(4), 354–361.

Khalil, H.K. (2002). *Nonlinear Systems.* Prentice Hall, 3rd edition.

Khatib, O. (1987). A unified approach for motion and force control of robot manipulators: The operational space formulation. *IEEE J. Robot. Automat.*, 3(1), 43–53.

Maggiore, M., Loría, A., and Panteley, E. (2023). Reduction theorems for stability of compact sets in time-varying systems. *Automatica*, 148.

Meyer, C.D. (1970). Generalized inverses of block triangular matrices. *SIAM J. Appl. Math.*, 19(4), 741–750.

Nakanishi, H. and Yoshida, K. (2006). Impedance control for free-flying space robots -basic equations and applications-. In *Proc. 2006 IEEE/RSJ Int. Conf. Intell. Robots Syst.* Beijing, China.

Ott, C., Dietrich, A., and Albu-Schäffer, A. (2015). Prioritized multi-task compliance control of redundant manipulators. *Automatica*, 53, 416 – 423.

Schmidt-Didlaukies, H., Pettersen, K.Y., and Sørensen, A.J. (2018). Modeling of articulated underwater robots for simulation and control. In *Proc. 2018 IEEE/OES Auton. Underwater Vehicles.* Porto, Portugal.

Sæbø, B.K., Pettersen, K.Y., and Gravdahl, J.T. (2022). Robust task-priority impedance control for vehicle-manipulator systems. In *Proc. 2022 IEEE Conf. Control Technol. Appl.* Trieste, Italy.

Umetani, Y. and Yoshida, K. (1989). Resolved motion rate control of space manipulators with generalized Jacobian matrix. *IEEE Trans. Robot. Autom.*, 5(3), 303–314.

Wu, X., Ott, C., Albu-Schäffer, A., and Dietrich, A. (2022). Passive decoupled multitask controller for redundant robots. *IEEE Trans. Control Syst. Technol.*, 31(1), 1–16.